# OCT-based arterial elastography: robust estimation exploiting tissue biomechanics

**R.C. Chan**[*1,2], **A.H. Chau**[*1,4], **W.C. Karl**[3], **S. Nadkarni**[1,2], **A.S. Khalil**[4],
**N. Iftimia**[1,2], **M. Shishkov**[1,2], **G.J. Tearney**[1,2], **M.R. Kaazempur-Mofrad**[4], **and**
**B.E. Bouma**[1,2]

[1]*Wellman Center for Photomedicine, Mass. General Hospital, Boston, MA 02114*
[2]*Harvard Medical School, Boston, MA 02115*
[3]*Dept. of Electrical Engineering & Computer Engineering, B.U., Boston, MA 02215*
[4]*Dept. of Mechanical Engineering, M.I.T., Cambridge, MA 02139*
*rchan@nmr.mgh.harvard.edu, *alyx@mit.edu (co-first-authors)*

**Abstract:** We present a novel multi-resolution variational framework for vascular optical coherence elastography (OCE). This method exploits prior information about arterial wall biomechanics to produce robust estimates of tissue velocity and strain, reducing the sensitivity of conventional tracking methods to both noise- and strain-induced signal decorrelation. The velocity and strain estimation performance of this new estimator is demonstrated in simulated OCT image sequences and in benchtop OCT scanning of a vascular tissue sample.

© 2004 Optical Society of America

**OCIS codes:** (100.2960) Image analysis; (170.4500) Optical coherence tomography

---

## References and links

1. G.C. Cheng, H.M. Loree, R.D. Kamm, M.C. Fishbein, R.T. Lee, "Distribution of circumferential stress in ruptured and stable atherosclerotic lesions. A structural analysis with histopathological correlation," Circulation **87**(4), 1179-1187 (1993).
2. R.T. Lee, C. Yamamoto, Y. Feng, S. Potter-Perigo, W.H. Briggs, K.T. Landschulz, T.G. Turi, J.F. Thompson, P. Libby, T.N. Wight, "Mechanical strain induces specific changes in the synthesis and organization of proteoglycans by vascular smooth muscle cells," J. Biol. Chem. **276**, 13847-51 (2001).
3. M.R. Kaazempur-Mofrad, H.F. Younis , S. Patel, A.G. Isasi, R.C. Chan, D.P. Hinton, R.T. Lee, R.D. Kamm, "Cyclic Strain in Human Carotid Bifurcation and its Potential Correlation to Atherogenesis: Idealized and Anatomically-Realistic Models," Journal of Engineering Mathematics **47**(3-4), 299-314 (2003).
4. R.T. Lee, F.J. Schoen, H.M. Loree, M.W. Lark, P. Libby, "Circumferential stress and matrix metalloproteinase 1 in human coronary atherosclerosis. Implications for plaque rupture," Arterioscler. Thromb. Vasc. Biol. **16**, 1070-1073 (1996).
5. J. Ophir, E.I. Cspedes, H. Ponnekanti, Y. Yazdi, and X. Li, "Elastography: A quantitative method for imaging the elasticity in biological tissues," Ultrason. Imag. **13**(2), 111134 (1991).
6. C.L. de Korte, A.F.W. van der Steen, E.I. Cespedes, G. Pasterkamp, S.G. Carlier, F. Mastik, A.H. Schoneveld, P.W. Serruys, N. Bom, "Characterization of plaque components and vulnerability with intravascular ultrasound elastography," Phys. Med. Biol. **45**, 1465-1475 (2000).
7. M.M. Doyley, F. Mastik, C.L. de Korte, S.G. Carlier, E.I. Cespedes, P.W. Serruys, N. Bom, A.F.W. van der Steen, "Advancing intravascular ultrasonic palpation toward clinical applications," Ultrasound in Med. & Biol. **27**(11), 1471-1480 (2001).
8. J.A. Schaar, C.L. de Korte, F. Mastik, C. Strijder, G. Pasterkamp, E. Boersma, P.W. Serruys, A.F.W. van der Steen, "Characterizing vulnerable plaque features with intravascular elastography," Circulation **108**, 1-6 (2003).
9. I.K. Jang, B.E. Bouma, D.H. Kang, et al., "Visualization of coronary atherosclerotic plaques in patients using optical coherence tomography: comparison with intravascular ultrasound," J Am Coll Cardiol. **39**, 604609 (2002).

#4660 - $15.00 US
(C) 2004 OSA

Received 25 June 2004; revised 25August 2004; accepted 13 September 2004
20 September 2004 / Vol. 12, No. 19 / OPTICS EXPRESS 4558

10. J.M. Schmitt, "Optical Coherence Tomography (OCT): a review," IEEE Journal of Selected Topics in Quantum Electronics **5**(4), 1205-1215 (1998).
11. J.M. Schmitt, "OCT Elastography: Imaging microscopic deformation and strain of tissue," Optics Express **3**, 199-211 (1998), http://www.opticsexpress.org/abstract.cfm?URI=OPEX-3-6-199.
12. D.D. Duncan, S.J. Kirkpatrick, "Processing algorithms for tracking speckle shifts in optical elastography of biological tissues," Journal of Biomedical Optics **6**(4), 418-426 (2001).
13. D.D. Duncan, S.J. Kirkpatrick, "Performance analysis of a maximum-likelihood speckle motion estimator," Optics Express **10**(18), 927-941 (2002), http://www.opticsexpress.org/abstract.cfm?URI=OPEX-10-18-927.
14. J. P. Lewis, Fast Template Matching, Vision Interface, 120-123 (1995).
15. D. Huang, E.A. Swanson, C.P. Lin, et al., "Optical coherence tomography," Science **254**, 11781181 (1991).
16. G.J. Tearney, M.E. Brezinski, B.E. Bouma, et al., "In vivo endoscopic optical biopsy with optical coherence tomography," Science **276**, 20372039 (1997).
17. B.E. Bouma, G.J. Tearney, "Power-efficient nonreciprocal interferometer and linear-scanning fiber-optic catheter for optical coherence tomography," Opt Lett. **24**, 531533 (1999).

## 1. Introduction

Atherosclerotic plaque biomechanics determine the distribution of stress concentration within the arterial wall [1]. Cyclic mechanical strain also affects macrophage gene expression and smooth muscle cell proliferation within the vessel wall [2, 3]. Histological studies have shown that matrix metalloproteinases weaken the structural integrity of plaques and localize in regions of high circumferential stress, suggesting links between plaque biomechanics and increased susceptibility to mechanical disruption [4]. Detailed characterization of arterial wall biomechanics may therefore provide complementary information about lesion stability that is not readily available from conventional vascular imaging.

Since ultrasound-based tissue elastography for biomechanical strain imaging was first pioneered by Ophir *et al.* [5], considerable effort has been invested in the development of intravascular ultrasound (IVUS) based coronary arterial elastography [6, 7, 8]. Today, IVUS elastography is the only method that has been demonstrated clinically for strain characterization in coronary lesions. In IVUS elastography, one-dimensional A-lines from a single short-axis cross-section are acquired as the artery pulsates over the cardiac cycle. Consecutive A-lines in time, corresponding to the same circumferential vessel location, are selected starting from a cardiac phase with minimal catheter motion artifact. Arterial tissue displacements as a function of the luminal pressure change are estimated with cross-correlation analysis and the corresponding one-dimensional strains are computed from the tissue velocity gradient. In current practice, IVUS elastography is capable of acquiring approximately 500 angles per revolution, with an imaging depth of $\sim$7.5 mm, and a spatial resolution of 200 $\mu$m for axial strains (oriented along each A-line). The spatial resolution of IVUS elastography is a significant limitation since vulnerable atherosclerotic plaques have structural components, e.g., fibrous caps, on the order of 50-200 $\mu$m in dimension, meaning that a thin fibrous cap will fall entirely within a single sample.

Optical coherence tomography (OCT) has an order of magnitude higher spatial resolution and significantly enhanced soft tissue contrast relative to IVUS [9], at the cost of reduced imaging depths. Vascular optical coherence elastography (OCE) has the potential to provide high-resolution characterization of strains in tissue lying within 1.0-1.5mm of the lumen interface, the region most susceptible to plaque disruption. In OCT-based elastography, strain measurements could be made every 10 microns allowing for 5 to 20 sample measurements through the thin fibrous cap. This larger number of samples in OCT-based imaging and elastography potentially allows for better definition of both structural geometry and biomechanical characterization relative to IVUS-based methods.

Successful development of intravascular OCE requires robust arterial tissue velocimetry, a critical step necessary for subsequent strain or elastic modulus estimates. Unfortunately how-

ever, OCT-based elastography is challenging because the short optical wavelengths used result in rapid noise- and strain-induced decorrelation of intensity patterns between consecutive image frames. Motion tracking based on a frozen speckle assumption [11, 12, 13] is inadequate for vascular OCE, particularly for structures on the size scale of arterial walls.

In this paper, we present a multi-resolution algorithm which incorporates prior knowledge about arterial wall behavior within a variational energy formulation for robust estimation of tissue motion and strain in two-dimensions. We demonstrate the performance of this novel estimator in simulated OCT images of a tissue block undergoing deformation. With these simulations, we have been able to examine not only velocity estimation errors, but also strain estimation errors, which have not been addressed in prior work on OCT-based elastography [11, 12, 13]. Finally, we present an example of estimation from benchtop OCT imaging of a normal arterial specimen imaged *ex vivo*.

## 2. Optical coherence elastography: background and related work

Optical coherence elastography is based on the same principles as those underlying ultrasound elastography. As tissue is imaged under mechanical loading, displacement occurs in image features that primarily correspond to macroscopic architecture, e.g., tissue interfaces. In addition, motion occurs in coherent imaging speckle since the spatial distribution of microscopic tissue scatterers changes under loading. The estimation of motion from macroscopic architecture and microscopic speckle assumes that image features are well-preserved between consecutive images. The desired velocity estimate will therefore maximize similarity measures between blocks in a reference image and those in a search image acquired under different loading conditions.

As described by Schmitt [10, 11], interference images obtained in OCT can be approximated by the product of an exponential decay term which models beam attenuation and a spatial convolution,

$$I(x,y) = \exp(-2\bar{\mu}_s y)\left[\sigma_b(x,y) * h(x,y)\right] \tag{1}$$

Coordinates $x$ and $y$ correspond to lateral and axial scan directions, respectively oriented perpendicular and parallel to the sample beam axis. Parameter $\bar{\mu}_s$ is the mean attenuation due to scattering over the sample, $\sigma_b(x,y)$ models backscattering in the sample as a distribution of points with varying backscattering cross-sections, and $h(x,y)$ represents the OCT system point spread function (PSF). The OCT PSF can be approximated as a separable and spatially invariant product between the source autocorrelation function, $\Gamma(y)$, and the pupil function, $p(x)$, of the source-detection optics [11],

$$h(x,y) = \Gamma(y)p(x) \tag{2}$$

For Gaussian beams,

$$\Gamma(y) = \mathrm{Re}\left[\langle \mathbf{E}_s(y')\mathbf{E}_s(y'+y)\rangle\right] = \exp\left(-\left(\frac{\pi y}{\sqrt{\ln 2}}\frac{\Delta\lambda}{\lambda_0^2}\right)^2\right)\cos\left(2\pi y/\lambda_0\right) \tag{3}$$

and

$$p(x) = \exp\left[-\frac{1}{2}\left(\frac{\pi D x}{\lambda_0 f}\right)^2\right] \tag{4}$$

where $\mathbf{E}_s$ is the vector electric field amplitude of the source, $\lambda_0$ is the central free-space wavelength of the source, $\Delta\lambda$ is the FWHM spectral bandwidth of the source, $f$ is the focal length of the objective lens, and $D$ is the $1/e^2$ intensity diameter of the sample beam at the entrance pupil of the objective lens.

Based on this image formation model, a single point scatterer undergoing displacement from position $(x_0, y_0)$ in the reference image to a new position $(x_0 + u, y_0 + v)$ in the search image, will have corresponding reference and search interference images described by:

$$I_R(x,y) = \exp(-2\bar{\mu}_s y)\left[\sigma_b \delta(x-x_0, x-y_0) * h(x,y)\right]$$
$$= \exp(-2\bar{\mu}_s y)\left[\sigma_b h(x-x_0, y-y_0)\right] \tag{5}$$

$$I_S(x,y) = \exp(-2\bar{\mu}_s y)\left[\sigma_b \delta(x-x_0-u, x-y_0-v) * h(x,y)\right]$$
$$= \exp(-2\bar{\mu}_s y)\left[\sigma_b h(x-x_0-u, y-y_0-v)\right] \tag{6}$$

With conventional velocimetry, tissue motion is estimated by maximizing the correlation coefficient between sub-blocks of either the envelopes or complex magnitudes of Eq. (5)-(6) [9]. Each image is subdivided into blocks of predefined size. For each reference block, cross-correlations with all search image blocks are computed to obtain correlation coefficients as a function of relative displacement between the reference and search locations. The best matching block in the search image will maximize the normalized cross-correlation function and the relative offset between this block and the reference provides the desired velocity estimate. This procedure is expressed mathematically in Eq. (7)-(8) for a reference position of $(x,y)$ and $M \times N$ sub-blocks with mean intensities of $\mu_R$ and $\mu_S$. In Eq. (7), the estimated lateral and axial displacements, $\hat{u}$ and $\hat{v}$, at a given $(x,y)$ location, are the arguments of the normalized correlation function $\rho_{x,y}(u,v)$ which maximize the correlation coefficient. Overlapping sub-blocks can be used to estimate velocities on a finer grid in the reference image.

$$[\hat{u} \quad \hat{v}] = \arg\max_{[u \quad v]} \rho_{x,y}(u,v) \tag{7}$$

$$\rho_{x,y}(u,v) = \frac{\int_{-M/2}^{M/2}\int_{-N/2}^{N/2}\left[I_R(x'-x,y'-y)-\mu_R\right]\left[I_S(x'-x-u,y'-y-v)-\mu_S\right]dx'dy'}{\left[\int_{-M/2}^{M/2}\int_{-N/2}^{N/2}[I_R(x'-x,y'-y)-\mu_R]^2 dx'dy' \int_{-M/2}^{M/2}\int_{-N/2}^{N/2}[I_S(x'-x-u,y'-y-v)-\mu_S]^2 dx'dy'\right]^{1/2}} \tag{8}$$

For the case of a translating impulse scatterer, velocity estimation with Eq. (5)-(8) basically tracks the shift in the impulse response when $\bar{\mu}_s y \approx \bar{\mu}_s(y+v)$. For real tissues containing ensembles of scatterers undergoing non-rigid deformation, the coherent impulse response from each scatterer produces interference patterns in the backscattered signal that may not simply translate between sequential images in time. Velocity estimates become more sensitive to interference noise which reduces the maximum achievable correlation coefficient in Eq. (8). Decorrelation effects such as this occur whenever the correlation window size is large relative to the deforming structures of interest or when the strain induced by loading is large. In both cases, the effects of mechanical loading cannot be modeled by simple speckle translation since spatial distortion occurs in the underlying scatterer distribution. Under realistic circumstances, imaging noise and decorrelation not only reduce the correlation value at the true displacement within the correlation surface $\rho_{x,y}(u,v)$, but also introduce jitter which shifts the location of correlation peaks in addition to multiple local maxima or false peaks whose values can exceed the correlation at the true displacement. As a result, velocity and strain estimates can be excessively noisy for characterizing biomechanical properties.

## 3. Robust optical coherence elastography

Strategies for improving velocity estimation include image sequence blurring for noise suppression, the use of larger correlation windows, and smoothing of velocity fields after estimation by

correlation maximization. Based on our observations, these strategies lead to limited improvements in velocity and strain estimates while compromising the spatial resolution advantage of OCT for elastography. Image sequence blurring can remove not only noise, but also fine image features that may be useful in motion tracking. Large correlation windows reduce our ability to track fine changes in the velocity field and also lead to a violation of the translating speckle model that is assumed in Eq. (7)-(8). Filtering of velocities or strains either with median-filters or other smoothing kernels operate on the measurements after they have already been made. This approach therefore cannot make use of information present within the underlying correlation functions to improve velocity and strain estimates. A better solution would be to take a "data-driven" approach in which velocity filtering takes place during the correlation maximization process itself. In this manner, all the available correlation data are taken into consideration for robust velocity estimation. One such scheme is the variational method we describe below.

### 3.1. A variational framework for incorporation of prior knowledge

We have posed the velocity estimation problem as a variational energy minimization in order to exploit velocity information present within the correlation functions while adding robustness to estimation by incorporating prior knowledge about velocity fields in the pulsating arterial wall. In this approach, we avoid image smoothing so as to preserve all available information from the full resolution data. The overall variational energy functional is

$$E(V(x,y)) = aE_D(V(x,y)) + bE_S(V(x,y)) + cE_I(V(x,y)) \tag{9}$$

This energy depends on the unknown velocity field $V(x,y) = [\ u(x,y)\quad v(x,y)\ ]$ and is a weighted combination of three terms which control data fidelity, $E_D(V(x,y))$, strain field smoothness, $E_S(V(x,y))$, and arterial wall incompressibility, $E_I(V(x,y))$. The functional forms for each of these terms are:

$$E_D(V(x,y)) = -\int\int \rho_{x,y}(V(x,y))dxdy \tag{10}$$

$$E_S(V(x,y)) = \int\int \left\| \nabla^2 V(x,y) \right\|^2 dxdy \tag{11}$$

$$E_I(V(x,y)) = \int\int \left\| \nabla \cdot V(x,y) \right\|^2 dxdy \tag{12}$$

where the expression $\rho_{x,y}(V(x,y))$ in Eq. (10) is the correlation coefficient function shown in Eq. (8). Minimizing the data fidelity term in the absence of the strain smoothness and tissue incompressibility terms is the same as correlation function maximization and results in velocity estimates that are identical to those from conventional velocimetry. The strain smoothness and tissue incompressibility terms constrain velocity estimation to penalize deviations based on prior knowledge about arterial tissue biomechanics. Information in correlation functions from neighboring reference locations is effectively combined to confer robustness to decorrelation, false peaks, and poorly-defined regions of elevated correlation coefficient values. The strain smoothness term forces the second derivative of the arterial velocity fields to vary smoothly over the wall whereas the incompressibility model couples the behavior of the u and v velocity fields so that points inside the wall do not deviate far from incompressibility. The desired velocity field estimate, $\hat{V}(x,y)$, will minimize the overall variational energy:

$$\hat{V}(x,y) = \underset{V(x,y)=[\ u(x,y)\quad v(x,y)\ ]}{\arg\min} \{aE_D(V(x,y)) + bE_S(V(x,y)) + cE_I(V(x,y))\} \tag{13}$$
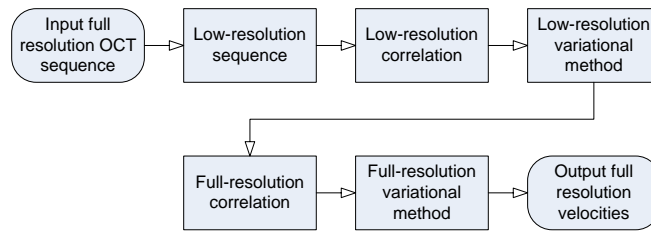
Fig. 1. Block diagram illustrating multi-resolution velocity field estimation

### 3.2. Multi-resolution numerical solution for convergence to a global minimum

In order to obtain a numerical solution to the energy minimization problem, we discretize the continuous expressions in Section 3.1 and derive the evolution equations corresponding to the first variation of the energy functional. Starting from an initial guess for the velocity fields, the resulting matrix-vector equations are solved iteratively until the maximum magnitude change falls below 0.01%. Since this solution process will converge to a local minimum of the variational energy function, the unknown velocity fields must be initialized close to the global minimum to ensure good global convergence properties. In order to achieve this, we use a multi-resolution approach illustrated as a block diagram in Fig. 1.

The full resolution reference and search images are first downsampled by a factor of 5 to obtain a low-resolution sequence from which an initial low-resolution estimate of the velocity field is obtained by correlation maximization in Eq.( 7)-(8). This estimate is used to initialize the variational method applied at the low-resolution scale. The resulting robust estimates of the low-resolution velocity distribution are mapped into the high-resolution domain and are used to define high-resolution search regions for computing full-resolution correlation functions at each reference position of interest. The low-resolution estimates from the variational method also serve as a good initial guess for iterative estimation of velocity fields from the full-resolution correlation functions. The resulting full-resolution velocity estimates are then used for strain calculations as described in Section 6.

Both the conventional and multi-resolution variational algorithms described above were implemented in C++ for rapid processing. MATLAB (MathWorks, Natick, Massachusetts, USA) was also used for image visualization and data analysis. To achieve rapid computation on the order of seconds for an image pair, we used a fast normalized cross-correlation approximation to the correlation coefficient function in Eq. (8) that uses 2D FFTs to compute the numerator and pre-computed running sums for the denominator [14].

## 4. Simulations of OCT imaging during tissue compression

We characterized the performance of the multi-resolution variational method in simulated OCT imaging during axial compression of a tissue block containing a circular inclusion (Fig. 2(a)) which represents either a typical compliant lipid pool or a stiff calcified nodule. Sequential interference images were generated as described in Eq.(1)-(6) by computing the product of an exponential decay term and a convolution between the coherent OCT point spread function and the distribution of backscattering arising from point scatterers moving in the sample.

The scattering fields in these simulations were generated by assigning backscattering values at discrete points within the tissue block. These backscattering values derived from independent uniform random variables with a variance of 10 for scatterers within the block and a variance of 2 for scatterers within the circular inclusion. These values were empirically chosen to produce

higher mean backscattering within the block relative to the inclusion. The resulting contrast difference emulates that observed between lipid and the normal arterial wall in OCT images.

Motion of the tissue scatterers during compression was simulated using displacement fields from finite element modeling of the tissue geometry. A two-dimensional rectangular geometry with an embedded circular inclusion was defined. Since lipid pools and calcified nodules can range in size from a few hundred microns to over a 1.0mm in dimension, a typical inclusion diameter of 500 $\mu$m, falling within the biologically relevant range, was chosen for these simulations. Fixed-point boundary conditions were imposed at the center of the bottom edge of the block and roller boundary conditions were assigned at all other points on the bottom edge. An axial (downward) displacement load was applied to the top surface so that the block was compressed by 0.15mm over 5 timesteps, to achieve an overall strain of 4.3%. With each timestep, the load induced $\sim$0.9% strain within the block.

Both the block and inclusion were modeled as nearly incompressible linear elastic materials ($v$=0.495). For all simulations, the block was assigned unit elastic modulus, while the inclusion modulus was varied to represent a lipid rich or calcific lesion embedded in fibrous tissue. The modulus ratio of lipid to fibrous plaque is approximately 0.0001, and the modulus ratio of calcium to fibrous plaque is approximately 5 [3]. Finite element modeling was performed in ADINA 8.0 (Watertown, MA), using a mesh composed of 9-node, quadrilateral, 2D, plane strain elements. The mesh density, defined by the edge length of each element, was 0.025 mm in and around the inclusion and 0.1 mm in the surrounding block (Fig. 2(b)). Each simulation model consisted of approximately 3200 elements and 13000 nodes. The displacement fields computed at each time step were used to represent tissue scatterer velocities,$u(x,y)$ and $v(x,y)$, between sequential OCT frames. The backscattering field, $\sigma_b(x,y,t+1)$, associated with moving tissue scatterers at time $t+1$ was computed using the equation

$$\sigma_b(x,y,t+1) = \sigma_b(x-u(x,y),y-v(x,y),t) \tag{14}$$

In practice, the tissue scatterer field in the first frame was first upsampled and then non-uniformly resampled with linear interpolation in Eq.(14) to obtain tissue scatterer fields in sequential frames.

Using the coherent PSF approximation in Eq.(2)-(4), we simulated a PSF based on measurements of the axial fringe pattern of our OCT system (Fig. 3(a)). Convolution of this coherent PSF with tissue scatterer fields from Eq.(14) was followed by multiplication with an axial exponential decay and downsampling to obtain a sequence of simulated images $I(x,y,t)$ with a pixel size of 1 $\mu$m by 25 $\mu$m. The degree of speckle or multiplicative noise present in these
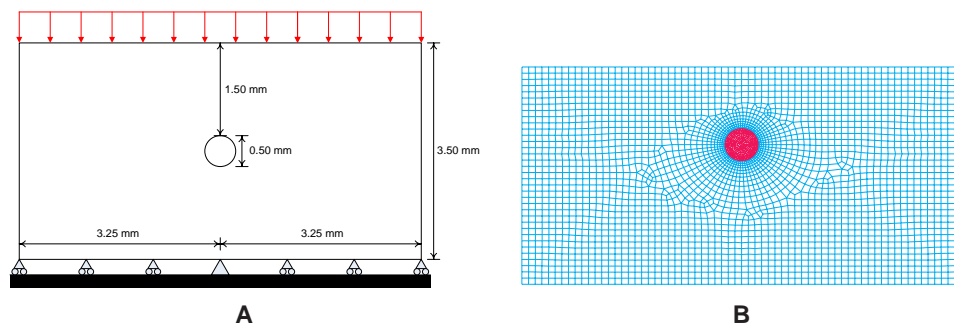


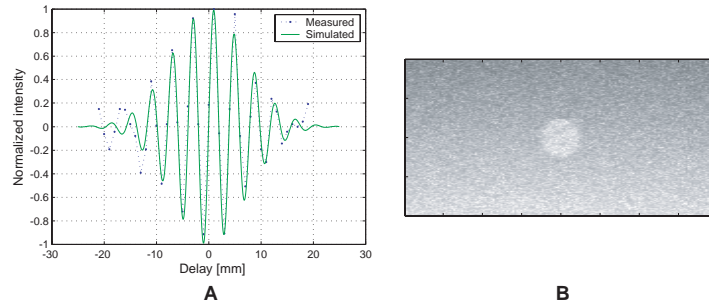Fig. 2. (a) Finite element geometry. (b) Finite element mesh.

Fig. 3. (a) A comparison of a simulated PSF with fringe measurements from our OCT system, (b) OCT image simulation of an inclusion within a tissue block after demodulation.

simulations was further controlled by using the noise model

$$I_n(x,y,t) = I(x,y,t) + nI(x,y,t) \tag{15}$$

where $n$ is a uniformally-distributed random variable with zero mean and variance $\sigma_n^2$. An example of OCT image simulation following demodulation with the Hilbert transform is shown in Fig. 3(b).

## 5. Vascular tissue imaging

Our system for time-domain OCT (TD-OCT) imaging has been described in detail previously [15, 16, 17]. This TD-OCT system provides an intrinsic spatial resolution of 10 $\mu m$ axially and 25 $\mu m$ laterally. For vascular imaging *ex vivo*, we used this system in benchtop scanning (XY) mode. Light from a broadband optical source with a center wavelength of 1310 nm and a bandwidth of 70 nm is split into a reference arm and sample arm within an interferometer. The field in the sample arm is focused through the scanning optics to probe tissue at a depth corresponding to the optical pathlength of the reference arm. Backscattered light returning from the sample arm mixes with the field from the reference arm to produce an interference signal that is then digitized. The amplitude of the interference signal carries information about tissue structure and optical properties at the scan depth defined by the reference arm. To capture the fringe-resolved information within the interference signal, oversampling is performed at 1 $\mu$m intervals axially and 25 $\mu$m intervals laterally, with 12 bit quantization for each sample. Tissue structure in an XY cross-section is probed in the axial (Y) direction by varying the optical pathlength of the reference arm and in the lateral (X) direction by sweeping the sample beam across the specimen. In this manner, image frames consisting of 2500 axial samples by 500 lateral samples are acquired in 250 ms.

A normal segment of human aorta harvested from autopsy was warmed to 37°C in phosphate buffered saline. Imaging was performed within 24 hours of harvesting. The cylindrical aortic segment was sectioned longitudinally and opened to obtain a rectangular tissue specimen with the luminal surface exposed to the sample beam. The longitudinally cut ends were affixed to a sample holder so that mechanical loading in the lateral direction would approximate circumferential stretching of the intact aortic segment. The specimen was mounted horizontally within the sample holder so that one end was rigidly fixed while the other end was affixed to a micromanipulator that allows for one-dimensional translation along the horizontal axis (Fig. 4). The total specimen length was 50mm and the width was 20mm. The specimen length between the tissue clamps was 30mm, whereas the imaging field-of-view was 10mm laterally and approx

1.5mm axially. The imaging position within the sample was monitored by visualizing an aiming beam (laser diode, 635 nm) that was coincident with the sample beam. Scans were positioned within the center of the specimen and the scan direction within the sample arm was aligned so that scatterer displacements were confined within the imaging plane.

## 6. Results and discussion

For conventional velocity estimation based on correlation maximization, each correlation function was upsampled with bi-cubic interpolation by a factor of 50 around the peak in order to detect subpixel shifts of 0.02 $\mu$m axially and 0.5 $\mu$m laterally. A reference block size of $81 \times 7$ pixels ( $81 \times 175$ $\mu$m) and a search region of $361 \times 21$ pixels ($361 \times 525$ $\mu$m) were used to compute correlation functions for the conventional method. These parameters were empirically determined to balance the need for sensitivity to spatial variations in velocity against the need to minimize errors in velocity estimation. Median filtering of velocity and strain estimates from conventional motion tracking was performed with a $5 \times 5$ kernel prior to comparisons with results from the variational approach.

For the low-resolution step of the variational method, a reference block size of $15 \times 11$ pixels ($75 \times 1375$ $\mu$m) and a search region of $61 \times 41$ pixels ($305 \times 5125$ $\mu$m) were used to compute each correlation function. At full-resolution, a reference block size of $25 \times 7$ pixels ($25 \times 175$ $\mu$m) and a search region of $101 \times 21$ pixels ($101 \times 525$ $\mu$m) were used. Weighting parameters for the variational approach were empirically determined to be a $= 1$ , b $= 20$, and c $= 0.1$ based on visual examination of processing results from a subset of simulated OCT sequences. These values were then used for velocity estimation in the OCT experiments described below.

Following velocity estimation, the deformation matrix $F$ was calculated at every point in the velocity field using first-order finite difference approximations to the expression

$$F = \left[ \begin{array}{cc} 1 + \frac{\partial u}{\partial x} & \frac{\partial u}{\partial y} \\ \frac{\partial v}{\partial x} & 1 + \frac{\partial v}{\partial y} \end{array} \right] \tag{16}$$

The deformation matrix is related to the strain matrix $E$ and the identity matrix $I$ by the relationship

$$E = \left[ \begin{array}{cc} \varepsilon_{xx} & \varepsilon_{xy} \\ \varepsilon_{xy} & \varepsilon_{yy} \end{array} \right] = \frac{1}{2} \left( F^T + F - 2I \right) \tag{17}$$

if a small strain approximation is assumed. For simulated OCT imaging of axial compression, we present results for the axial strain component $\varepsilon_{yy}$ of the strain matrix whereas for imaging experiments with lateral stretching, we present results for the lateral strain component $\varepsilon_{xx}$ (strains are reported in units of %). Errors in velocity and strain field estimates were evaluated
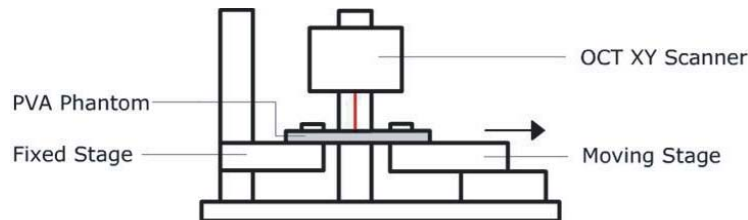


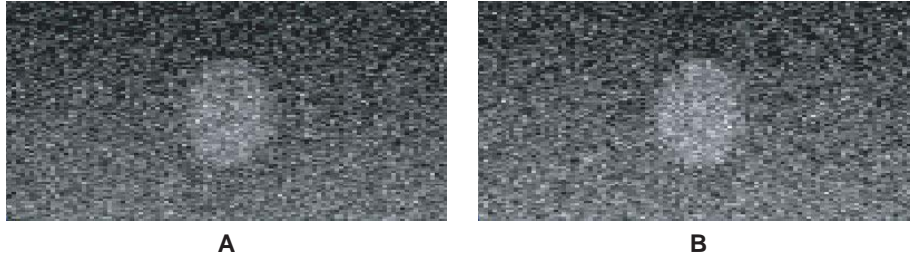Fig. 4. Benchtop OCT imaging system for XY scanning of mechanically-loaded specimens.

**A**                                      **B**

Fig. 5. Movie clips showing simulated axial compression (vertical loading in the downward direction) of a 500$\mu$m inclusion with (a) more compliant (464KB Quicktime movie) and (b) stiffer material properties than the surrounding tissue block (464KB Quicktime movie).

based on the normalized root-mean-squared error measures

$$\mathrm{RMS}_{\mathrm{velocity}} = \sqrt{\frac{1}{N}\sum_{k=1}^{N}\left(\frac{v_k - v_{k,\mathrm{real}}}{v_{k,\mathrm{real}}}\right)^2} \quad \mathrm{RMS}_{\mathrm{strain}} = \sqrt{\frac{1}{N}\sum_{k=1}^{N}\left(\frac{\varepsilon_k - \varepsilon_{k,\mathrm{real}}}{\varepsilon_{k,\mathrm{real}}}\right)^2} \quad (18)$$

where $N$ is the total number of estimates, $v_k$ and $v_{k,\mathrm{real}}$ are the estimated and real axial or lateral velocities, and $\varepsilon_k$ and $\varepsilon_{k,\mathrm{real}}$ are the estimated and real axial or lateral strains at the $k^{\mathrm{th}}$ point of interest within the velocity field.

### 6.1.   Simulation experiments

We examined the detectability of a 500$\mu$m inclusion as a function of noise-induced speckle decorrelation and compared the RMS error in axial velocity and strain estimates from conventional motion estimation relative to those from robust estimation. Values for $v_{k,\mathrm{real}}$ and $\varepsilon_{k,\mathrm{real}}$ were obtained directly from finite element modeling. Velocities were reported in units of pixels with positive axial and lateral velocities corresponding respectively to downward and rightward displacement.

Figure 5 illustrates simulated axial compression of approximately 0.9% strain for two tissue blocks, one with a compliant inclusion and the other with a stiff inclusion. On visual inspection, gross tissue displacement in both movie clips appears to be occurring in the downward direction with velocities decreasing in magnitude from top to bottom. Differences in inclusion stiffness between these examples are extremely difficult to appreciate by visual examination alone, emphasizing the need for computational methods to measure tissue velocities and strains. Decorrelation in speckle patterns between image frames can be visualized and its severity can be measured by using the average value of correlation coefficient maxima over the image field. For these movie sequences, the mean correlation peak is approximately 0.95.

Figure 6-7 illustrate the FEM-derived axial velocity fields corresponding respectively to the compliant and stiff inclusion movie sequences. In addition, they show the axial component of velocity measurement results from conventional motion tracking and robust estimation within the variational framework. For these examples, the estimated velocity fields from both methods are qualitatively similar to the true velocity from FEM. The estimated velocity fields also demonstrate that processing of the movie sequences in Fig. 5 is necessary to highlight the differences in behavior that could not be appreciated visually between compliant and stiff inclusions. The estimate from the variational approach appears significantly smoother than that from conventional tracking. Additionally, the axial velocity RMS error is greater from conventional velocimetry than from robust estimation. For the stiff inclusion, the RMS error in the axial velocity field was 1.60% from conventional velocimetry whereas the RMS error with ro-
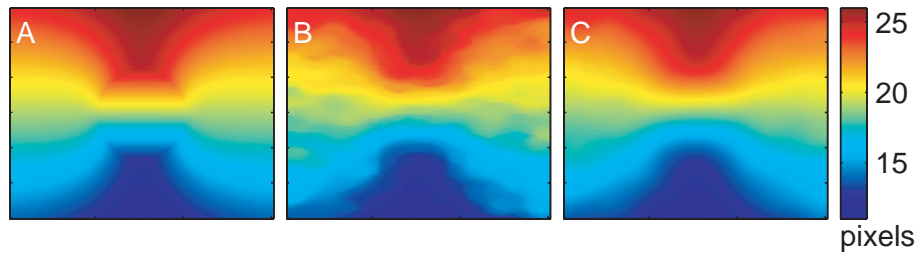
Fig. 6. Axial velocity fields for a compliant inclusion. (a) True axial velocities from finite element modeling. (b) Axial velocity estimates from conventional motion tracking. c) Axial velocity estimates from multi-resolution variational method. Axial compression was applied in the downward direction.
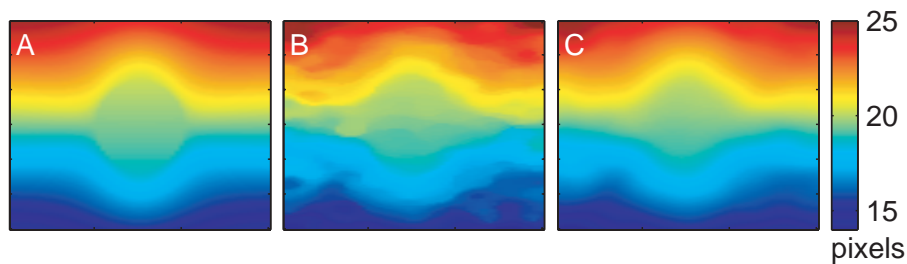


Fig. 7. Axial velocity fields for a stiff inclusion. (a) True axial velocities from finite element modeling. (b) Axial velocity estimates from conventional motion tracking. c) Axial velocity estimates from multi-resolution variational method. Axial compression was applied in the downward direction.

bust estimation was 1.04%. Similar results were obtained from the compliant inclusion (1.83% for the conventional approach vs 1.40% for the variational approach).

Figure 8-9 show the corresponding axial strain fields for both inclusion simulations. The effect of velocity noise on strain field measurements is clearly evident from these examples. While estimates from conventional and robust velocimetry were both qualitatively similar to the FEM-derived displacements, the strain estimates are less similar to the true strain. Axial strain is the derivative of the axial velocity field, therefore any noise present in the velocity estimate is accentuated in the strain image due to the high-pass characteristics of the derivative operator. Even with median-filtering, it is difficult to fully appreciate the extent and magnitude of the strain difference within the inclusion for strains derived from conventional motion tracking. In contrast, it is possible to determine the location and size of the inclusion with robust strain estimation. Furthermore, it is possible to visually distinguish the compliant inclusion from stiff inclusion with the variational approach. Quantitatively, the difference in RMS strain error between the conventional and variational methods is marked. In the stiff inclusion, for example, with the conventional approach, the RMS strain error is 109.1% whereas with the variational method, RMS strain error is 27.5%. Strains derived from conventional tracking are challenging to interpret whereas robust estimation allows for easier and more accurate interpretation of strains measurements for comparisons between lesion types.

In the presence of worsening noise conditions or large tissue strains relative to imaging frame rate, decorrelation of speckle patterns occurs leading to a drop in the average value of correlation coefficient maxima over the image. Figure. 10-11 illustrate the effect of noise-induced
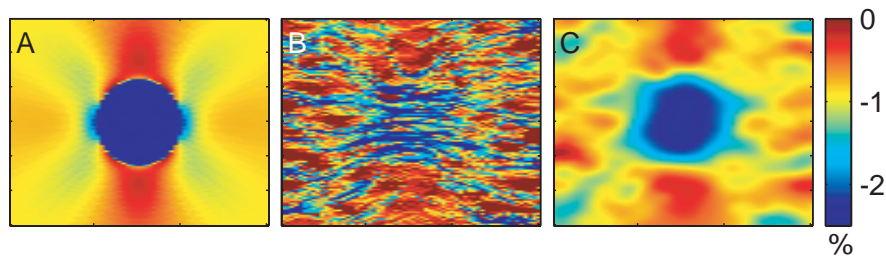
Fig. 8. Axial strain fields for a compliant inclusion. (a) True axial strains from finite element modeling. (b) Axial strain estimates from conventional motion tracking. c) Axial strain estimates from multi-resolution variational method. Axial compression was applied in the downward direction.
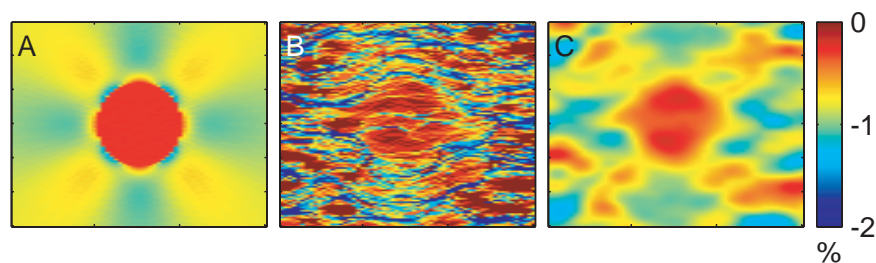


Fig. 9. Axial strain fields for a stiff inclusion. (a) True axial strains from finite element modeling. (b) Axial strain estimates from conventional motion tracking. c) Axial strain estimates from multi-resolution variational method. Axial compression was applied in the downward direction.

decorrelation on lesion detectability for robust estimation and on RMS estimation errors for both techniques. Decorrelation in these simulations was introduced by using the speckle noise model described previously and the averaged peak correlation coefficient was used to measure decorrelation.

In Fig. 10, we see that as the mean correlation peak drops from 0.95 to 0.54, the strain fields increasingly deviate from the known strain distribution due to increasing levels of noise and other estimation artifacts. At a correlation value of 0.54, the presence of an inclusion within the strain field is difficult to perceive even when robust estimation is used. In Fig. 11(a), we see that the RMS velocity error for both the conventional and variational methods decreases as the level of correlation increases. Velocity estimation errors with the robust approach are significantly lower than those from conventional estimation over the range of noise conditions examined. In Fig. 11(b), the corresponding strain estimation errors are shown. Again, errors decrease as correlation increases, with significantly larger RMS strain errors for the conventional method relative to the variational method. Strain errors for the stiff inclusion were lower than 50% only when correlation values were greater than 0.7 and when the robust estimator was used. Strain errors well in excess of 100% were observed for conventional estimation over the range of noise conditions studied.

## 6.2. *Imaging experiments*

In these imaging experiments, we examined velocity and strain estimation in a normal aortic specimen under either static or lateral stretching conditions. For the static case, the ground-truth
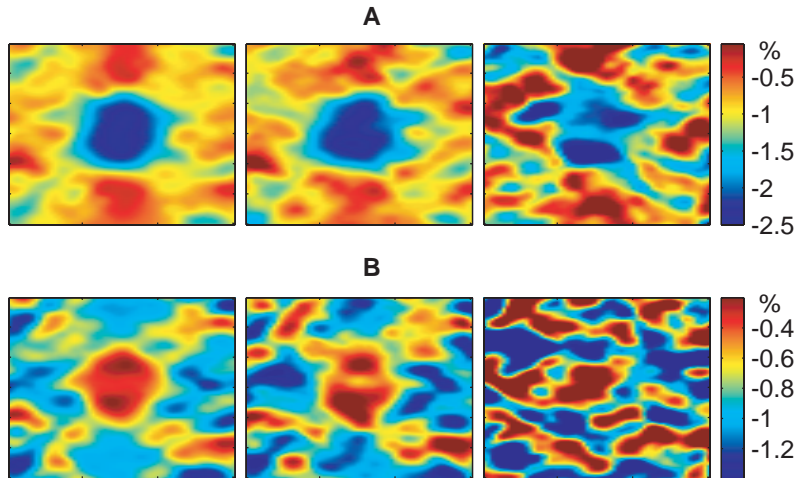
**A**



**B**



Fig. 10. Lesion detectability as a function of noise-induced decorrelation for (a) the compliant inclusion (correlation coefficients are 0.95, 0.79, 0.54 from left to right respectively) and (b) the stiff inclusion (correlation coefficients are 0.95, 0.81, 0.55 from left to right respectively).
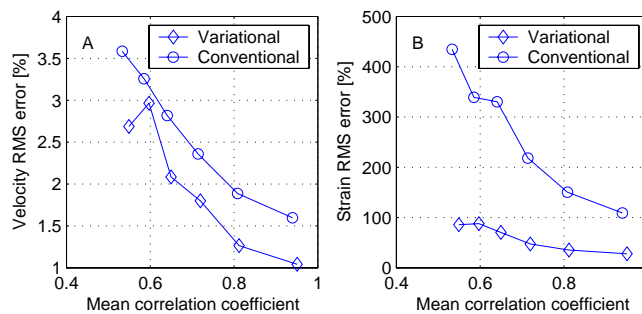


Fig. 11. Estimation errors in the stiff inclusion: (a) Root-mean-square velocity estimation error as a function of noise-induced decorrelation. (b) Root-mean-square strain estimation error as a function of noise-induced decorrelation.

velocity and strain fields should both be zero. Therefore, we determine the deviation of velocity and strain estimates away from zero as one measure of performance. For the case of lateral stretching, the expected strain distribution is homogenous and we report the standard deviation of estimated strains as a measure of strain homogeneity within the sample.

Under static conditions, the estimated mean lateral velocity with the conventional approach was 0.17 $\mu$m per frame compared with a nominal applied translation of 0 pixels per frame. The standard deviation of the lateral velocity estimates over the field was 3.94 $\mu$m per frame. In the axial direction, the mean and standard deviation were 0.66 $\mu$m and 4.28 $\mu$m, respectively. Velocity estimation with the variational approach showed a mean velocity of 0.0017 $\mu$m per frame laterally (0.54 $\mu$m per frame axially), which was closer to the applied translation than the results from the conventional method. The velocity standard deviation of 0.16 $\mu$m per frame laterally (0.58 $\mu$m per frame axially) was also smaller than for the conventional method results. The mean and standard deviation of strain estimates over the field were respectively 0.043%
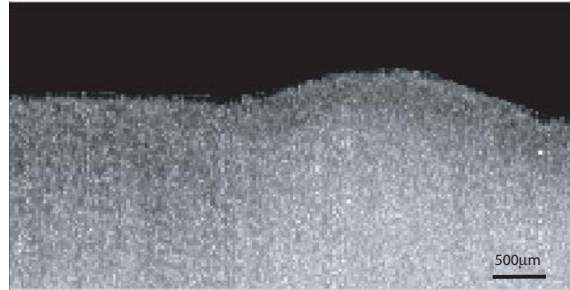
Fig. 12. OCT imaging of an aortic specimen undergoing lateral (right-to-left) motion (568KB Quicktime movie). Regions of the image outside the aorta have been masked out.

and 5.5% laterally (0.24% and 11.26% axially) for the conventional approach, compared with a nominal applied strain of 0% over the field. In contrast, robust estimation provides better strain estimation performance. The mean and a standard deviation of strain estimates were 0.0038% and 0.12% laterally (0.024% and 0.12% axially), respectively. Figure 12 shows a movie of the
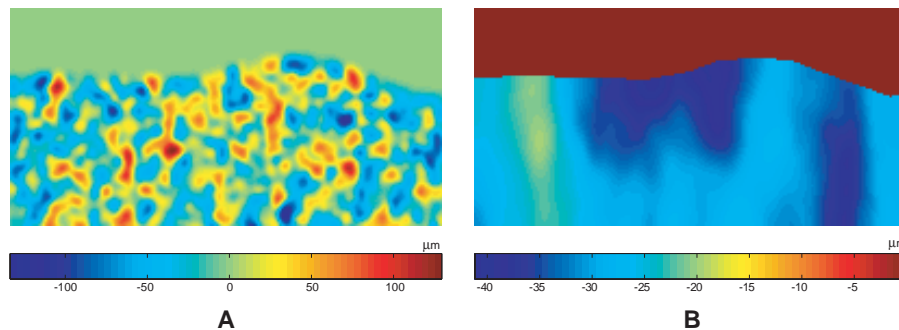


Fig. 13. Estimated lateral velocity fields for an aortic specimen undergoing lateral stretching (right-to-left in the imaging plane) a) from the conventional method, and b) from the variational method.

aortic segment undergoing lateral translation with slight lateral stretching. Figure 13 illustrates the lateral component of the velocity field measurement whereas Fig. 14 illustrates the lateral component of the estimated strain field. Velocities from robust estimation were observed to vary more smoothly in both the lateral and axial directions than estimates from conventional estimation. For the conventional approach, the strain mean and strain standard deviation were 0.22% and 47.26% in the lateral direction and 3.46% and 85.08% in the axial direction. In contrast, the strain field from robust estimation showed a mean and a standard deviation of 0.026% and 1.32% in the lateral direction and 0.02% and 0.14% in the axial direction. These results indicate that estimates from robust strain measurement are more consistent with the expected homogeneous strain field than those from conventional strain measurement. Further experimentation is underway to optimize and validate the accuracy and precision of velocity and strain estimates with the variational method.

## 7. Conclusions

We have developed a robust method of tissue velocity and strain estimation based on a variational framework that incorporates prior knowledge about tissue biomechanics. This estimator
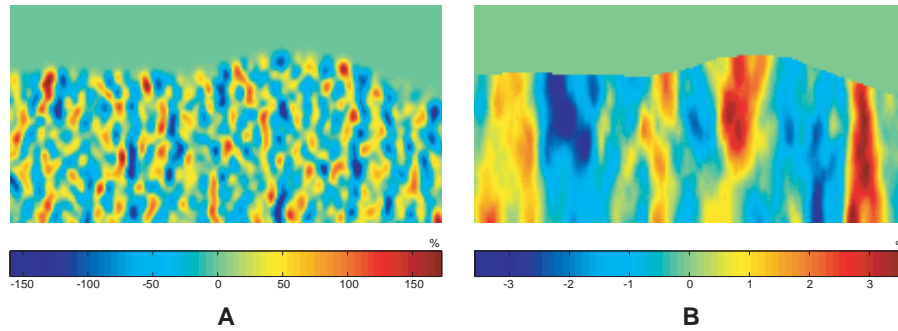
Fig. 14. Estimated lateral strain fields for an aortic specimen undergoing lateral stretching (right-to-left in the imaging plane) a) from the conventional method, and b) from the variational method.

outperforms conventional velocity and strain measurements based on correlation maximization. Our new approach provides accurate velocity estimates with lower RMS velocity errors than those from conventional methods over the range of imaging noise conditions studied. Strain estimation with the robust approach allows for strain measurements with an RMS strain error of less than 50% in simulated OCT sequences with correlation values higher than 0.7. The RMS strain estimation error with this method is lower than that from conventional estimation over the range of imaging conditions examined. The estimated strain fields from robust estimation allow for easier visual assessment of inclusion location, extent, and stiffness when compared with results from conventional methods. Finally, we have demonstrated robust velocity and strain estimation from images of a moving aortic specimen. Despite the lack of ground-truth in this case, our results indicate that the estimated velocity and strain fields from robust estimation are more consistent with the expected distribution of velocity and strains than those measurement with the conventional approach. Variational estimation of tissue velocity and strain therefore enables characterization of vascular tissue biomechanics *ex vivo* in a manner that has not been possible with existing techniques.

**Acknowledgments**